

Coupling Plasma-Synthesized N-Doped Graphene With Ice Templated Porous Electrode for Enhanced Aluminum Battery Performance

Downloaded from: https://research.chalmers.se, 2026-11-24 19:43 UTC

Citation for the original published paper (version of record):

Chen, R., M. Santhosh, N., Zavašnik, J. et al (2026). Coupling Plasma-Synthesized N-Doped Graphene With Ice Templated Porous Electrode for Enhanced Aluminum Battery Performance. Small, In Press. http://dx.doi.org/10.1002/smll.76627

N.B. When citing this work, cite the original published paper.

research.chalmers.se offers the possibility of retrieving research publications produced at Chalmers University of Technology. It covers all kind of research output: articles, dissertations, conference papers, reports etc. since 2004. research.chalmers.se is administrated and maintained by Chalmers Library

(article starts on next page)

Check for updates

Small

NANO · MICRO small
www.small-journal.com

RESEARCH ARTICLE OPEN ACCESS

Coupling Plasma-Synthesized N-Doped Graphene With Ice Templated Porous Electrode for Enhanced Aluminum Battery Performance

Ruiqi Chen[1] | Neelakandan M. Santhosh[2] | Janez Zavašnik[2] | Komal Gola[1] | Nitish Kumar[1] | Uta Klement[1] | Eva Kovacevic[3] | Elena Tatarova[4] | Ana Ferraria[5,6] | Vincenzo Palermo[1,7] | Uroš Cvelbar[2] | Jinhua Sun[1]

[1]Division of Materials and Manufacture, Department of Mechanical Engineering, Chalmers University of Technology, Göteborg, Sweden | [2]Department of Gaseous Electronics (F6), Jožef Stefan Institute, Ljubljana, Slovenia | [3]GREMI UMR7344, CNRS & University of Orleans, Orleans, France | [4]Instituto de Plasmas e Fusão Nuclear, Instituto Superior Técnico, Universidade de Lisboa, Lisboa, Portugal | [5]Institute for Bioengineering and Biosciences, Departamento de Engenharoa Quimica, Instituto Superior Técnico, Universidade de Lisboa, Lisboa, Portugal | [6]Associate Laboratory i4HB—Institute for Health and Bioeconomy at Instituto Superior Técnico, Universidade de Lisboa, Lisboa, Portugal | [7]Institute for Organic Synthesis and Photoreactivity (ISOF), CNR, Bologna, Italy

Correspondence: Uroš Cvelbar (uros.cvelbar@ijs.si) | Jinhua Sun (jinhua@chalmers.se)

Received: 25 April 2026 | **Revised:** 26 September 2026 | **Accepted:** 28 October 2026

Keywords: aluminum batteries | graphene | N-graphene | plasma doping | porous electrode

ABSTRACT

Rechargeable aluminum batteries are promising for next-generation energy storage owing to the low cost and abundance of aluminum. Graphene is an attractive cathode due to its high surface area and electrical conductivity, but its performance is limited by difficult production and sheet aggregation, which restrict electrolyte accessibility and ion transport. This study employs a plasma-enabled synthesis approach to produce both pristine graphene and nitrogen-doped graphene (N-graphene), followed by an ice templating strategy to directly construct a three-dimensional porous N-graphene electrode. The effects of nitrogen doping and porous electrode architecture are systematically investigated by comparing dense and porous electrodes. Nitrogen-doping increases the specific capacity by ~50%, from 36.24 to 54.4 mAh/g at a current density of 0.1 A/g. Furthermore, introducing porous structure provides an additional ~20% improvement, achieving a capacity of 65.5 mAh/g under the same conditions. This enhanced performance of porous electrode is attributed to its interconnected pores and partially aligned graphene sheets, which improve electrolyte accessibility and facilitate the adsorption and transport of $AlCl_4^-$ anions. The robust porous structure of N-graphene ensures excellent cycling stability, with no noticeable capacity decay over 5000 cycles. Coupling nitrogen doping with porous electrode architecture provides an effective strategy to enhance graphene-based aluminum batteries.

1 | Introduction

The rapidly increasing global demand for sustainable and clean energy has intensified research efforts to develop high-performance energy storage technologies. Lithium-ion batteries (LIBs) currently dominate the rechargeable battery market due to their high energy density, long cycle life, and low self-discharge rates [1, 2], enabling their widespread commercialization [3]. However, LIBs are not considered a fully sustainable solution due to their high cost, safety concerns, dependence on critical raw

Ruiqi Chen and Neelakandan M. Santhosh contributed equally to this work.

This is an open access article under the terms of the Creative Commons Attribution License, which permits use, distribution and reproduction in any medium, provided the original work is properly cited.
© 2026 The Author(s). *Small* published by Wiley-VCH GmbH

materials, and the environmental impacts associated with their production and end-of-life processing [4–6]. Consequently, the development of alternative energy storage systems has become a major focus in electrochemical energy storage [7–9]. Among emerging metal-ion batteries, aluminum-based batteries have attracted significant attention due to the exceptional volumetric and gravimetric capacities of aluminum (8040 mAh/cm^3 and 2980 mAh/g, respectively), along with its natural abundance, low cost, and rapid charging capability [10, 11]. In addition, aluminum is nonflammable, nontoxic, and air-stable, making it a safe and environmentally benign candidate for large-scale energy storage applications [12]. Room-temperature ionic liquids are widely used as electrolytes in non-aqueous aluminum batteries due to their wide electrochemical window, low vapor pressure, and high ionic conductivity [13]. However, direct intercalation of aluminum cations into conventional cathode materials is thermodynamically unfavorable [14]. Instead, aluminum-containing anions-typically $AlCl_4^-$ in ionic liquid systems composed of aluminum chloride ($AlCl_3$) and 1-ethyl-3-methylimidazolium chloride ([EMIm]Cl)-serve as the primary charge carriers [15].

Graphite has been extensively investigated as a cathode material for aluminum batteries due to its ability to reversibly intercalate $AlCl_4^-$ anions, delivering a specific capacity of approximately 66 mAh/g at 66 mA/g [15]. However, efficient intercalation requires highly crystalline graphite, and its limited interlayer spacing (~0.33 nm) restricts rapid ion diffusion, resulting in sluggish redox kinetics. In this context, graphene—an atomically thin carbon material derived from graphite—has emerged as a promising alternative due to its large specific surface area, high electrical conductivity, excellent reversibility, and electrochemical stability [16, 17]. Nevertheless, practical application of graphene is hindered by sheet aggregation during electrode fabrication, leading to disordered structures, reduced accessible active sites, and limited electrolyte accessibility for efficient $AlCl_4^-$ storage and transport.

Recently reported graphene-based cathodes rely on graphene oxide (GO) or reduced graphene oxide (RGO), which contain abundant defects and oxygen functional groups that impede anion intercalation [18]. In some cases, high-temperature annealing (e.g., ~2850°C) has been employed to restore graphene crystallinity by removing these functional groups [19]; however, such processes are energy-intensive and economically impractical for large-scale applications. Although chemical vapor deposition (CVD) can produce high-quality graphene, its limited yield and scalability—particularly in powder form—restrict its applicability in aluminum batteries [20, 21]. In contrast, plasma-enabled synthesis has emerged as a promising alternative, enabling rapid and controllable production of graphene with tunable morphology and orientation, either on substrates or in powder form [22]. The interaction of plasma species with carbon nanostructures can also induce defects, heteroatom doping, and functionalization, thereby creating additional active sites for aluminum storage and offering new opportunities for material design [23, 24].

Unlike graphite, restacked graphene does not reconstruct into a highly ordered crystalline structure, resulting in a distinct charge-storage mechanism in aluminum batteries [8, 25]. One of the key strategies to enhance the electrochemical activity of graphene is heteroatom doping (e.g., with boron, nitrogen, or sulfur), which can modify the electronic structure and surface chemistry of graphene, introduce additional defect sites, and enhance the interaction between $AlCl_4^-$ and the carbon framework [26, 27]. For example, boron doping has been shown to introduce additional defects in RGO, improving both capacity and reaction kinetics [28]. Density functional theory studies suggest that aluminum anions exhibit strong binding affinity to nitrogen-doped graphene (N-graphene: N-Gr) [29]. Nitrogen doping can also modulate the electronic structure, enhancing conductivity while introducing defect sites for ion storage [30]. However, conflicting reports indicate that nitrogen dopants may also hinder anion intercalation [29, 31], highlighting the need for a controlled doping strategy to optimize cathodic charge-storage behavior in aluminum batteries [32, 33].

In addition to material chemistry, electrode architecture plays a critical role in governing electrolyte accessibility and ion transport, particularly in graphene-based electrodes, where sheet aggregation can severely limit the accessible surface area [34, 35]. Structural engineering on the electrode level, such as modification of the current collector and introduction of porous architectures, has been widely investigated to address these limitations [36–40]. A porous electrode can provide interconnected electrolyte pathways, increase the accessible electrode–electrolyte interface, and facilitate ion transport, thereby enhancing surface-driven charge storage and rate performance [13, 41]. They also help alleviate intercalation-induced stress by enabling surface-driven charge storage mechanisms [13, 42, 43]. One of such case is the excellent rate capability and cycling stability demonstrated by the three-dimensional GO aerogels [44]. However, porous structures engineered at the material level are often compromised during electrode fabrication processes such as slurry mixing, coating, and drying. This highlights the importance of constructing the porous architecture directly at the electrode level, where the pore structure can be preserved throughout electrode fabrication [38]. Such an architecture can simultaneously improve electrolyte accessibility, reduce graphene restacking, and provide continuous pathways for $AlCl_4^-$ transport. In particular, combining a porous electrode architecture with partially aligned graphene sheets can increase the accessibility of active sites while facilitating directional ion transport.

In this work, we combine one-step plasma synthesis and an ice-templating strategy to directly fabricate a three-dimensional porous graphene-based electrode, thereby avoiding structural degradation associated with conventional slurry processing. This approach enables efficient accommodation of ionic liquid electrolytes within the electrode, facilitating rapid adsorption/desorption and diffusion of $AlCl_4^-$ anions. As illustrated in Figure 1, graphene (Gr) and nitrogen-doped graphene (N-Gr) powders were synthesized via a one-step plasma-assisted method, with high quality and purity as reported [33, 45], followed by conventional slurry coating and directional freezing to construct the porous electrode architecture. The effects of material chemistry and electrode architecture are distinguished by comparing pristine graphene, dense N-Gr, and porous N-Gr electrodes. The stronger binding interaction between $AlCl_4^-$ and N-Gr results in enhanced specific capacity compared to pristine graphene. Additionally, the engineered porous architecture enhances electrolyte interactions and ion transport, thereby

16136829, 0, Downloaded from https://onlinelibrary.wiley.com/doi/10.1002/smll.76627 by Chalmers University Of Technology, Wiley Online Library on [13/11/2026]. See the Terms and Conditions (https://onlinelibrary.wiley.com/terms-and-conditions) on Wiley Online Library for rules of use; OA articles are governed by the applicable Creative Commons License

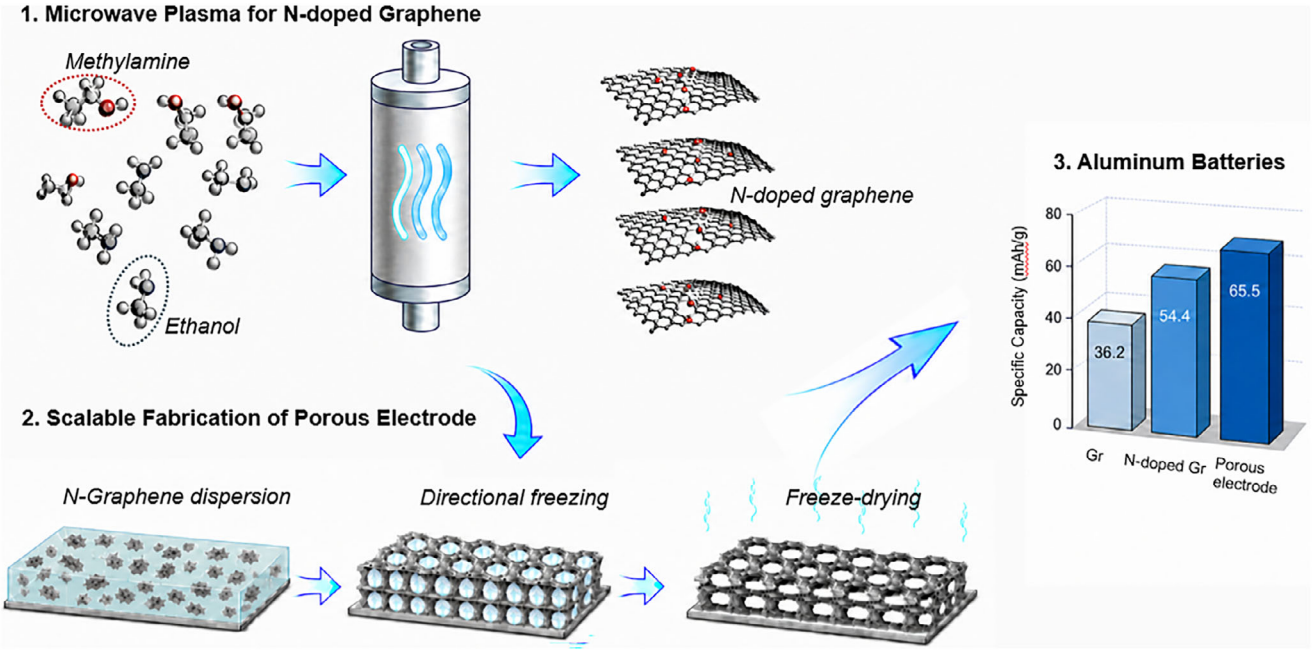


FIGURE 1 | Schematic illustration of the fabrication of N-doped graphene based porous electrode for improved performance of aluminum battery.

mitigating diffusion limitations. As a result, nitrogen doping increases the specific capacity by ~50% (from 36.24 to 54.4 mAh/g at 0.1 A/g), while the porous electrode design provides a further ~20% enhancement, achieving 65.5 mAh/g under the same conditions. The graphene porous structure promotes faster anion intercalation, leading to improved rate capability. Furthermore, the robust porous architecture ensures excellent cycling stability, with no noticeable capacity decay after 5000 cycles. Overall, this work demonstrates that coupling nitrogen-doped graphene chemistry with electrode-level porous architecture provides an effective strategy for enhancing the electrochemical performance of graphene-based aluminum battery cathodes.

2 | Experimental Methods

2.1 | One-step Plasma Synthesis of Graphene (Gr) and Nitrogen-Doped Graphene (N-Gr)

The direct synthesis of freestanding Gr and N-Gr powdered structures, which were the primary materials in this study, was performed in a surface-wave (SW)- induced microwave plasma at atmospheric pressure, as previously described [33, 45]. For the synthesis of free-standing graphene sheets, the microwave power is generated by a 2.45 GHz generator, with the output power varied from 500 to 2000 W. The plasma discharge takes place in a quartz reactor that comprises two sections: a small one with internal and external radii of 0.75 and 0.9 cm, respectively, connected via a conical section to a large tube with internal and external radii of 2.15 and 2.3 cm, respectively. The graphene nanosheets were synthesized using ethanol as carbon precursor and methylamine as nitrogen precursor (for N-Gr) in a mixture of argon, which was injected into the tube from the top. The operating parameters were: microwave power: 2 kW; ethanol flow rate: 35 sccm; argon flow rate: 1200 sccm; methylamine flow rate: 6 sccm. Both nanostructures were captured by a Hurricane Cyclone system, followed by a methanol trap. The detailed synthesis process is described in our previous reports [33, 46]. Besides, a low-pressure plasma system reported elsewhere [23, 24] was used to create defects in Gr and attain different nitrogen concentrations. The Gr powder was placed in a glass vial and positioned in the nitrogen plasma for N-doping with an N_2 flow of 100 sccm, plasma power of 100 W, and treatment times of 1 min and 5 min. For nitrogen-free defect creation, argon plasma was used for ion bombardment with an Ar flow of 100 sccm, a plasma power of 100 W, and a treatment time of 5 min.

2.2 | Electrodes Preparation and Fabrication of the Porous Electrode

The as-synthesized Gr and N-Gr powder and the plasma post-treated samples were mixed with the conductive additives (acetylene black) and styrene butadiene rubber and sodium carboxylmethyl cellulose (SBR/CMC mass ratio 1:1) as binder in the high-speed mixer (Kakuhunter SK-300S II) at a mass ratio of 80:10:10, using water as the solvent. A homogeneous slurry was obtained after 20 min of mixing at 1500 RPM. The slurry was then coated on the surface of molybdenum foil. The coated electrodes were dried in the vacuum oven at 80°C for at least 12 h. The electrodes are annotated by Gr-DE and N-Gr-DE. To form a porous structure with ordered nitrogen-doped graphene in the electrode, the slurry-coated electrode was first frozen at a controlled temperature to allow ice to grow from the bottom to the top surface. The porous structure was formed after removing the ice under vacuum for at least 24 h. The electrodes are annotated by N-Gr-PE. The areal mass loading of active materials is 1 mg/cm^2, the electrode thickness is ~50–500 μm. A schematic of the electrode fabrication that involves one-step plasma synthesis of Gr and N-Gr and the ice template porous electrode fabrication is presented in Figure 1.

16136829, 0, Downloaded from https://onlinelibrary.wiley.com/doi/10.1002/smll.76627 by Chalmers University Of Technology, Wiley Online Library on [13/11/2026]. See the Terms and Conditions (https://onlinelibrary.wiley.com/terms-and-conditions) on Wiley Online Library for rules of use; OA articles are governed by the applicable Creative Commons License

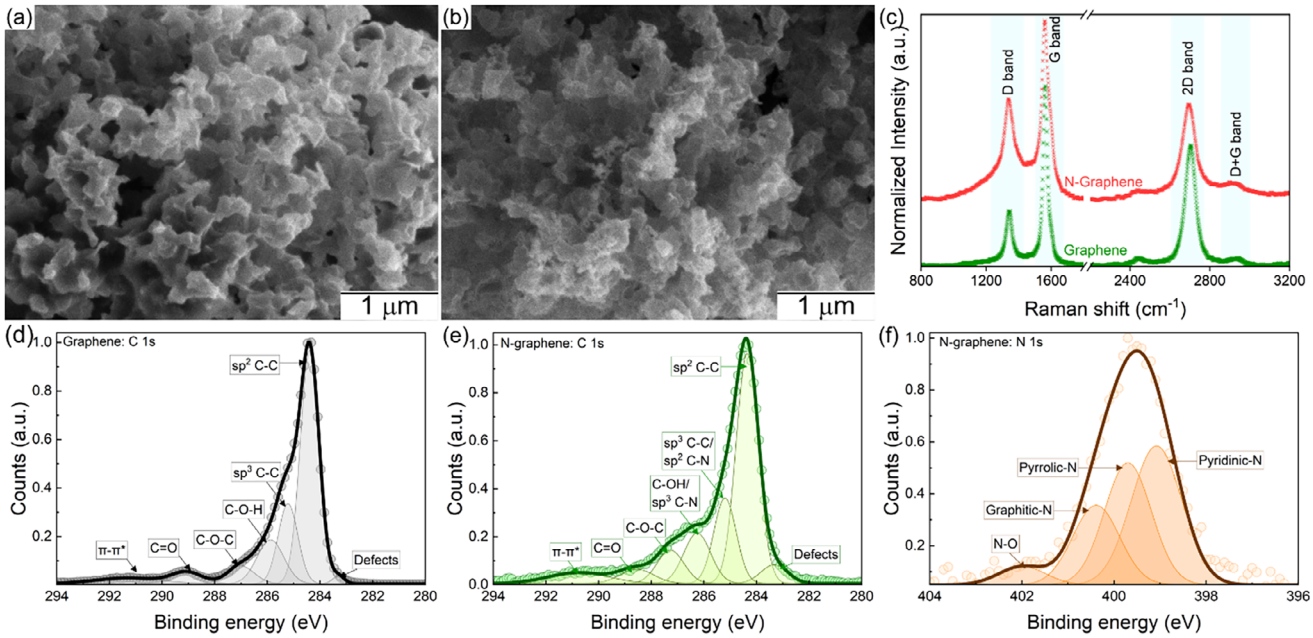


FIGURE 2 | Surface and structural analysis of plasma-synthesized Gr and N-Gr structures. SEM micrographs of plasma-synthesized (a) Gr, (b) N-Gr; (c) comparison of the Raman spectra analysis; Normalized high-resolution XPS C 1s spectra of (d) Gr, (e) N-Gr; (f) normalized high-resolution XPS N 1s spectra of N-Gr.

2.3 | Characterizations

The majority characterizations were carried out only on the Gr and N-Gr samples, which were considered as primary materials in this study. The morphology and structures of fabricated Gr and N-Gr were analyzed by scanning electron microscope (SEM, Verios 4G HP, Thermo Fisher Scientific), and porous electrodes were examined using SEM JEOL 7800F Prime. Transmission electron microscopy (TEM) was used to compare the nanoscale morphology, layer stacking, and local crystallinity of the plasma-synthesized Gr and N-Gr powders using a Talos F200X G^2 (Thermo Fisher Scientific) operated at 200 kV. The structural quality of Gr and N-Gr was analyzed by Raman spectroscopy (confocal Raman spectrometer; NTEGRA, NT-MDT) using an excitation wavelength of 488 nm at multiple points to evaluate the homogeneity. Surface elements and chemical composition of Gr and N-Gr were identified using X-ray photoelectron spectroscopy (XPS; PHI-TFA XPS spectrometer equipped with Al-monochromatic X-ray source at an energy of 1486.6 eV, Physical Electronics Inc. and KRATOS XSAM800 X-ray spectrometer with double anode, operating in Fixed Analyser Transmission mode). X-ray Diffraction (XRD, Discovery D8, Bruker) was used to characterize the lattice structure of graphene samples. The surface area, pore size, and volume distribution of dense electrodes and porous electrodes were measured using Brunauer–Emmett–Teller (BET) specific surface area analysis (Tristar 3000).

2.4 | Electrochemical Characterization

The as-prepared graphene-related electrodes were used as the cathode, aluminum foil as the anode, and glass fiber as the separator. The ionic liquid electrolyte with the composition of aluminum chloride ($AlCl_3$) and 1-ethyl-3-methylimidazolium chloride ([EMIm]Cl) with a molar ratio of 1.3:1 was used. The aluminum battery cell was then assembled using modified Swagelok-type cells in an argon-filled glove box. A molybdenum rod and a glassy carbon rod were used as the current collectors for the anode and cathode, respectively. The fabricated aluminum batteries were discharged/charged between 0.5 and 2.3 V at 0.1 A/g to 0.2, 0.5, 1, 2, 5 A/g using a Biologic battery cycler (BCS-805). Cyclic voltammetry (CV) was carried out between 0.5 and 2.3 V. Electrochemical impedance spectroscopy (EIS) was performed from 10^4 to 0.01 Hz.

2.5 | *Ex Situ* Characterization of Electrodes

The cells were disassembled in the argon-filled glove box when stopped at different potentials. The electrodes were then washed to remove the residual absorbed electrolyte. The washed electrodes were dried under vacuum before being used for *ex situ* Raman spectroscopy (confocal Raman spectrometer, WITec alpha300 R) and XPS measurements. The Raman spectra were recorded at 532 nm excitation across multiple points to evaluate homogeneity.

3 | Results and Discussion

3.1 | Structural Characterization and Chemical Composition Analysis

Plasma synthesis of Gr and N-Gr structures yielded a very lightweight powdered form, promising material for various electrical and electrochemical applications. Various surface analysis techniques were used to understand variations in the surface and chemical compositions of Gr and N-Gr. Surface morphology

16136829, 0, Downloaded from https://onlinelibrary.wiley.com/doi/10.1002/smll.76627 by Chalmers University Of Technology, Wiley Online Library on [13/11/2026]. See the Terms and Conditions (https://onlinelibrary.wiley.com/terms-and-conditions) on Wiley Online Library for rules of use; OA articles are governed by the applicable Creative Commons License

studies of the structures using SEM reveal that Gr and N-Gr display disordered sheets that entangle with each other (Figure 2a,b and Figure S1). Each nanosheet is illustrated with a wavy, wrinkled morphology. The major difference observed between the Gr and N-Gr structures is that the graphene nanosheets in N-Gr are more densely packed. High-resolution surface images are presented in Figure S1 to describe the wavy features of the plasma-synthesized nanostructures. To understand changes in the structural quality of graphene resulting from nitrogen incorporation, the samples were further analyzed by Raman spectroscopy. Both graphene structures illustrated the typical Raman characteristics of graphene (Figure 2c), and the major peaks were observed at 1341 (D band), 1564 (G band), 1603 (D' band), 2695 (2D band) and 2931 (D+G band) cm^{-1} [33, 47]. The G band is the in-plane vibrations of the sp^2 hybridized carbon, while the D band forms from the breathing mode of sp^2 carbon activated by defects. The presence of the shoulder peak at 1603 cm^{-1} could be due to the presence of the graphitic edges in both samples. An in-depth Raman analysis was conducted to assess the effect of nitrogen doping on the graphene lattice by comparing the D-to-G band ratio after deconvoluting the D and G bands (Figure S2). The changes in the defect ratio, from 0.35 in Gr to 0.56 in N-Gr, indicate that the degree of defects increased after the plasma treatment. The intensity relationship between G and 2D bands was altered, with the N-Gr showing a decay in 2D band intensity. This could be attributed to the more congested features observed from the SEM micrograph in N-Gr. Considering that both the Gr and N-Gr exhibited varying degrees of defects and sharp edges, this could facilitate intercalation reactions, ion storage and faster ion diffusion during electrochemical processes. TEM images show similarly thin, crumpled nanosheets in both Gr and N-Gr, with 1–5 layers (Figure S3a,b). Selected-area electron diffraction (SAED) confirms the preserved hexagonal sp^2 carbon framework after nitrogen incorporation (Figure S3c). The measured d_{100} and d_{110} spacings correspond with the theoretical values for graphitic carbon, indicating that the in-plane atomic arrangement remains unaffected by N-doping.

To further elucidate the changes in chemical composition, the materials were analyzed by XPS and the survey spectra of N-Gr feature peaks at around 284.4, 400, and 532 eV, corresponding to carbon, nitrogen, and oxygen, respectively (Figure S4a). The atomic concentration of nitrogen in N-Gr is approximately 8%. The comparison of high-resolution C 1s spectra of the Gr and N-Gr indicates peak broadening in the 286–288 eV region, implying changes in carbon bonding due to nitrogen incorporation into the carbon lattice (Figure S4b). The high-resolution C 1s spectra of Gr were deconvoluted into different components (Figure 2d): sp^2 C-C (284.4 eV), sp^3 C-C (285.2 eV), C-OH (286 eV), C-O-C (287 eV), C = O (289 eV), a π-π^* shake-up satellite (291.3 eV), and a small component around 283.3 eV, which corresponds to vacancy defects. The high-resolution C 1s spectra of N-Gr indicated that the peak area around 285–286 eV increased (Figure 2e), suggesting that carbon-nitrogen groups have formed due to plasma doping [48, 49]. Thus, the high-resolution N 1s was studied (Figure 2f), and the deconvolution of the peaks corresponds to pyridinic-N (399 eV; nitrogen at the edge), pyrrolic-N (399.7 eV, nitrogen in five-membered ring), graphitic-N (400.4 eV; substituted nitrogen) and the oxides of nitrogen (401.9 eV) [50]. This indicates that most of the nitrogen is incorporated with a sp^2 configuration, which preserves the structural quality of the material and acts as a defect center for aluminum storage. All surface analyses suggest that the produced Gr and N-Gr exhibit sharp edges and defect sites, which could facilitate ion storage and enhance the charge-storage mechanism. Thus, the plasma designed Gr and N-Gr were tested as efficient cathodes for aluminium batteries. The surface characteristics used to compare materials with different N-doping and Ar-plasma treatments are provided in the supporting information (Figure S5). In graphene-based electrodes, both the nitrogen concentration and configuration can influence electrochemical performance. Pyridinic-N and N–O groups have been reported to enhance the interaction with aluminium/chloroaluminate species [51]. In this study, the N-Gr contains a relatively high concentration of pyridinic-N and N–O groups, which may promote chloroaluminate adsorption and interfacial charge transfer, contributing to the enhanced capacity.

3.2 | Electrochemical Properties of Gr and N-Gr as Cathodes in Aluminum Batteries

Graphite has been commonly used as the cathode material for aluminum batteries due to its ability to accommodate the intercalated chloroaluminate anion ($AlCl_4^-$), and the storage mechanism can be described as [15]:

$$4Al_2Cl_7^- + 3e^- \rightarrow Al + 7AlCl_4^- \quad (1)$$

$$C_n + AlCl_4^- \rightarrow Cn[AlCl_4] + e^- \quad (2)$$

However, this charge-storage mechanism in highly crystalline graphite with aligned graphene layers differs from that in single-layer graphene. The graphene layers exhibit storage behavior for $AlCl_4^-$ based on surface adsorption and the interaction if the graphene layers are very well ordered in the electrode, making them suitable as active cathode materials for aluminum batteries. Apart from this, structural defects could also act as an active site for aluminum storage, and therefore, introducing defects in graphene with controllability is an efficient strategy for advancing the energy storage capabilities. One efficient strategy for introducing defects in the graphene lattice is heteroatom doping, and nitrogen doping is a key approach, given its higher binding energy with graphene [29, 35]. Therefore, to investigate the effect of doping on aluminum storage performance, the plasma-designed Gr and N-Gr were tested as cathodes for aluminum batteries.

The first-cycle galvanostatic charge-discharge curves of the Gr-DE and N-Gr-DE (8% nitrogen) electrodes at a current density of 0.1 A/g are presented in Figure 3a. No well-defined intercalation plateau can be observed, indicating that the energy storage mechanism of such graphene is different from that of graphite. The galvanostatic charge/discharge (GCD) curves show typical characteristics of surface adsorption of charge carriers. Although the charge-discharge curves of both samples show a similar shape, the specific capacity of the N-Gr-DE (54.4 mAh/g) is much higher than that of the Gr-DE (36.3 mAh/g). The results indicated that nitrogen doping can introduce defects, which act as additional ion storage sites, thereby improving the storage of $AlCl_4^-$.

16136829, 0, Downloaded from https://onlinelibrary.wiley.com/doi/10.1002/smll.76627 by Chalmers University Of Technology, Wiley Online Library on [13/11/2026]. See the Terms and Conditions (https://onlinelibrary.wiley.com/terms-and-conditions) on Wiley Online Library for rules of use; OA articles are governed by the applicable Creative Commons License

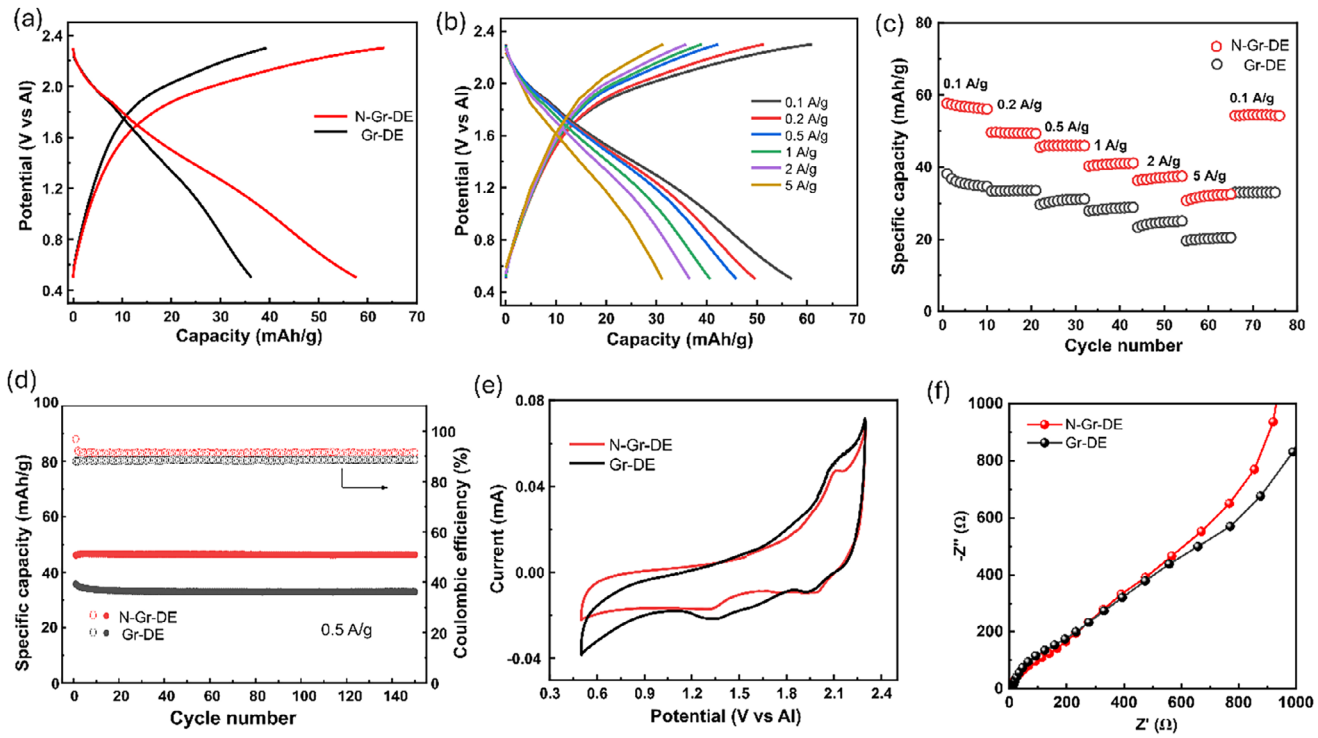


FIGURE 3 | Electrochemical performance of N-Gr-DE and Gr-DE: (a) The first cycle GCD profiles of Gr-DE and N-Gr-DE; (b) GCD profiles of N-Gr-DE for the first cycle at different current densities; (c) Rate capabilities of Gr-DE and N-Gr-DE; (d) Cycling performance and Coulombic efficiency of Gr-DE and N-Gr-DE at 0.5 A/g for 150 cycles; (e) Second cycle CV curves of Gr-DE and N-Gr-DE at a scan rate of 0.1 mV/s; (f) Nyquist plot from EIS measurements for Gr-DE and N-Gr-DE cathode.

In order to understand the effect of nitrogen doping on the diffusion of $AlCl_4^-$, the aluminum battery made by N-Gr-DE and Gr-DE cathodes was charged and discharged under different current densities from 0.1 A/g to 5 A/g. It can be observed that the specific capacity difference between N-Gr and Gr cathodes decreases as the current density increases, due to the sluggish diffusion and reaction of $AlCl_4^-$ in N-Gr-DE. The capacity decay rate of the N-Gr-DE is faster than that of the Gr-DE cathodes (the capacity difference at 0.1 A/g (21.4 mAh/g) is higher than the capacity difference at 5 A/g (10 mAh/g)), which agrees with the theoretical calculation that the binding energy of $AlCl_4^-$ to N-Gr is higher and that reversibility could be retarded. This could be improved by shortening the diffusion path of the $AlCl_4^-$ to the active materials and increasing the interaction between the electrolyte and electrode. It's worth noting that the N-Gr-DE can maintain a relatively higher specific capacity of 32 mAh/g (~60%) at the current density of 5 A/g, indicating a good performance for the graphene cathode after nitrogen doping (Figure 3b,c).

To distinguish the contribution of structural defects from that of nitrogen incorporation, graphene was treated with argon plasma to introduce defects without nitrogen doping and evaluated as a cathode for aluminum batteries. As shown in Figure S6, the Ar-plasma-treated graphene delivered a specific discharge capacity of approximately 30 mAh/g at 0.1 A/g, with a Coulombic efficiency of 75%. Its capacity decreased dramatically when the current density was increased to 0.5 A/g, indicating limited reaction kinetics and reversibility. Notably, the defect-rich graphene did not exhibit the enhanced electrochemical performance observed for N-Gr-DE, suggesting that defect generation alone is insufficient to account for the improved $AlCl_4^-$ storage and that nitrogen-containing sites play an additional role.

To further investigate the influence of nitrogen incorporation, two more N-Gr samples with different nitrogen contents (0.7 and 1.5 at%) were also evaluated (Figures S7 and S8). Both samples exhibited similar CV profiles, indicating comparable overall charge-storage behavior. However, their electrochemical performances differed substantially. N-Gr-0.7 delivered approximately 20 mAh/g with a Coulombic efficiency of 70% at 0.1 A/g, whereas N-Gr-1.5 exhibited a higher capacity of approximately 40 mAh/g and a Coulombic efficiency of 82% under the same conditions. For comparison, the optimized N-Gr-DE containing 8% N delivered 54.4 mAh/g. These results demonstrate that nitrogen incorporation and its concentration increase influence the electrochemical response of graphene toward $AlCl_4^-$ storage. However, the effect of nitrogen content cannot be considered independently of the associated changes in defect structure and local chemical environment. Therefore, the results support a combined contribution from nitrogen-containing active sites, porosity, and the defect-rich graphene structure, rather than attributing the enhanced capacity solely to defect density or nitrogen content.

The longevity of the electrodes is also key in aluminum batteries, and therefore, the cyclic stability of the Gr-DE and N-Gr-DE cathodes was tested at 0.5 A/g for 150 cycles and presented in Figure 3d. The N-Gr-DE cathode exhibits a higher capacity retention than the Gr-DE, nearly 100% for the former and 92.3%

16136829, 0, Downloaded from https://onlinelibrary.wiley.com/doi/10.1002/smll.76627 by Chalmers University Of Technology, Wiley Online Library on [13/11/2026]. See the Terms and Conditions (https://onlinelibrary.wiley.com/terms-and-conditions) on Wiley Online Library for rules of use; OA articles are governed by the applicable Creative Commons License

for the latter after 150 cycles. When comparing the Coulombic efficiencies of the two samples, N-Gr-DE shows a higher value (91.5%) than Gr-DE (88.5%). It has been reported that the low Coulombic efficiency may be due to side reactions, such as electrolyte decomposition [10, 52]. The relatively high Coulombic efficiency of N-Gr-DE indicates a stable solid-liquid interface, which provides a favorable basis for the reversible adsorption and reaction of $AlCl_4^-$ anions during the charge-discharge process.

The electrochemical behavior and the reaction pathways in Gr-DE and N-Gr-DE cathodes were further investigated by cyclic voltammetry (CV) at 0.1 mV/s, as shown in Figure 3e. The redox peaks for both electrodes display a similar feature, further confirming that their electrochemical behavior was primarily controlled by the physical adsorption and desorption of $AlCl_4^-$ [53]. However, the presence of small redox peaks indicates that intercalation also occurs, with anodic peaks at 2.1 V and two cathodic peaks at 1.9 and 1.3 V for the Gr-DE cathode, correlated with the intercalation/deintercalation of $AlCl_4^-$. Similarly, the N-Gr-DE cathode exhibits small peaks at 2.0 and 1.3 V, where the potential separation between anodic and cathodic peaks is comparably lower, demonstrating better reversibility for the intercalation/deintercalation of $AlCl_4^-$. Additionally, an additional cathodic peak was observed at 1.75 V, indicating a new deintercalation step after nitrogen doping and confirming that the electrochemical performance is a combined effect of physical adsorption and intercalation. The Nyquist plot illustrates the electrochemical impedance of the Gr-DE and N-Gr-DE electrodes (Figure 3f). When fitted with an equivalent circuit, the electrolyte resistance R_s is observed in the initial high-frequency region on the real axis, where the N-Gr-DE shows a lower value of 4.29 Ω than Gr-DE (6.00 Ω). The charge transfer resistance (R_{ct}) is indicated in the high and medium-frequency region [54], where the R_{ct} is higher for the Gr-DE cathode (1.32 kΩ) than that of N-Gr-DE (0.9 kΩ) (Table S1). The lower resistance in N-Gr-DE indicates a lower fitted interfacial impedance, which is consistent with improved interfacial charge transfer and effective ion accessibility. However, because the EIS response can contain contributions from electrolyte transport, electrode/electrolyte interfacial processes, contact resistance, and charge transfer, the R_{ct} values are not considered independent evidence of intrinsic electronic conductivity or reaction kinetics. Although the N-Gr-DE exhibited higher capacity at low current density as the cathode material for aluminum batteries, the higher binding energy of $AlCl_4^-$ to the N-Gr-DE may contribute to sluggish ion diffusion and poor rate performance at high current density. Therefore, an efficient strategy was implemented in this study to improve rate performance by developing electrodes with a porous structure, and the best-performing N-Gr-DE was used for further studies.

3.3 | N-Gr Porous Electrode for Aluminum battery

Using a template to produce porous graphene is a common method used for fabricating electrodes for batteries and supercapacitors with high-rate performance [7, 8, 25, 42, 43, 55, 56]. However, the fabricated porous structure might collapse or be destroyed upon dispersion of the binder in the solvent during slurry preparation for electrode fabrication. Thus, to improve the structural integrity, porous structures with graphene layers perpendicular to the electrode surface could be beneficial and would also allow fast intercalation of the $AlCl_4^-$ for the improved aluminum battery [57]. Here, using a controlled freeze-drying method, we proposed a fabrication of the porous electrode from N-Gr powder, which could not only increase the interaction between the electrolyte and the N-Gr surface area (Figure 1 and Figure S9) but also form an ordered graphene electrode, thereby allowing fast $AlCl_4^-$ diffusion and adsorption. After coating the slurry, the Molybdenum foil was placed on the cold metal plate (ca. −100°C) and immersed in liquid nitrogen. Because of the temperature gradient from the bottom to the top of the electrode, ice crystals grow vertically, concentrating the N-Gr and binder at their interfaces. Such a process will not only form 3D porous, conductive networks from N-Gr but also partially align the N-Gr nanosheets by pushing them to form the pore walls [42]. The surface morphology of the N-Gr electrode prepared by the standard slurry coating-drying process was observed from the SEM micrographs (Figure 4a–c). The standard slurry coating process illustrates a relatively dense surface (N-Gr dense electrode (N-Gr-DE)). The corresponding SEM micrographs of graphene with a surface morphology similar to that shown in Figure 4a are shown in Figure S10. Both show a dense surface, making it difficult for electrolytes to penetrate. As shown in Figure 4b,c, the fabricated porous electrode (N-Gr-PE) by the controlled freeze-drying method shows open pores on the surface of the current collector. The thickness of the pore wall is in the submicrometer range. The presence of the binder causes the Gr or N-Gr sheets to bind together, forming a relatively stable, mechanically robust structure. The total electrode thickness can be controlled from 50 to 500 μm, as shown in the cross-sectional SEM images (Figures S11 and S12). A relatively large N-Gr-PE, measuring 10 × 8.5 cm, was prepared for the demonstration (Figure S9). Under higher magnification (Figure 4c), it is noted that N-Gr sheets are packed with large pores around 5 μm in size. The XRD spectra of N-Gr-PE provide additional evidence for changes in the structural ordering of the graphene sheets (Figure 4d). Compared with N-Gr-DE and Gr, the (002) peak of N-Gr-PE at 26° exhibits higher intensity and a lower full width at half maximum (FWHM), suggesting a higher degree of structural ordering of the graphene sheets after the freeze-drying process [58]. Nitrogen adsorption-desorption measurements showed that the BET specific surface area increased from 71.44 m^2/g for N-Gr-DE to 92.04 m^2/g for N-Gr-PE (Figure 4e), demonstrating that the porous electrode architecture provides a higher accessible surface area. The formed 3D porous networks promise good electrical conductivity as cathodes, which is also desirable for achieving a high-rate performance.

To investigate the effect of the porous structure on the electrochemical performance of the N-Gr electrode for aluminum batteries, GCD cycles at 100 mA/g were performed, as shown in Figure 5a. Thanks to its porous structure, the specific capacity of the N-Gr porous electrode (N-Gr-PE) increases by 20%, from 54.4 to 65.5 mAh/g, compared with the N-Gr cathode with a dense electrode (N-Gr-DE). The shape of the GCD curves of both samples is similar without a plateau, indicating that the energy storage behavior is mainly governed by adsorption-desorption of $AlCl_4^-$. By taking advantage of the pores in the electrode, which can accommodate more electrolyte, $AlCl_4^-$ can be quickly absorbed and diffused within the electrode, resulting

16136829, 0, Downloaded from https://onlinelibrary.wiley.com/doi/10.1002/smll.76627 by Chalmers University Of Technology, Wiley Online Library on [13/11/2026]. See the Terms and Conditions (https://onlinelibrary.wiley.com/terms-and-conditions) on Wiley Online Library for rules of use; OA articles are governed by the applicable Creative Commons License

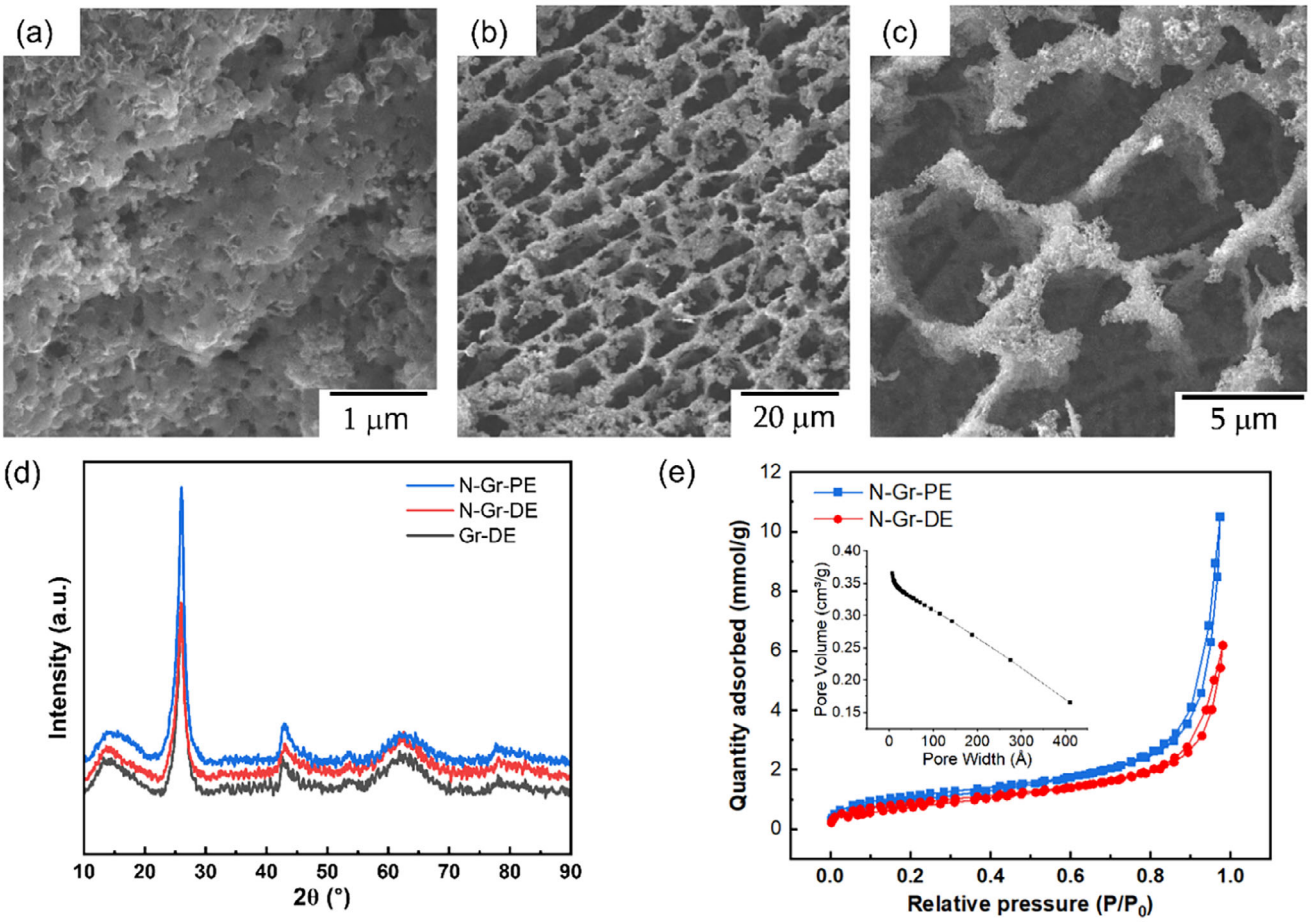


FIGURE 4 | Characteristics of N-Gr electrodes after conventional and freeze-drying process (a–c) surface morphology of (a) N-Gr-DE and (b,c) N-Gr-PE; (d) XRD spectra of Gr-DE, N-Gr-DE, and N-Gr-PE. (e) N2 adsorption/desorption isotherms of N-Gr-DE and N-Gr-PE.

in higher capacity. Compared with the N-Gr-DE prepared by the conventional slurry coating method, the porous electrode formed by controlled ice growth could also mitigate the aggregation of the 2D N-Gr sheet within the electrode, thereby resulting in a higher surface area for $AlCl_4^-$ storage [44]. As expected, the N-Gr-PE shows improved rate performance compared to N-Gr-DE (Figure 5b,c). The initial capacity difference at a low current density of 0.1 A/g is 5.16 mAh/g (10% improvement); it increases further to 5.9 mAh/g (18% improvement) at a relatively higher current density of 0.5 A/g, indicating that the porous structure in N-Gr-PE facilitates the fast diffusion of $AlCl_4^-$. The capacity difference decreases as the current density increases, from 0.5 A/g to 5 A/g. This might be due to the low diffusion rate of electrode, probably attributing to the thick electrode wall. Moreover, the specific capacity can be recovered to 62.3 mAh/g when the current density is reduced to 0.1 A/g, indicating good rate performance and durability in N-Gr-PE. The long-term cycling stability is examined using the GCD process over 150 cycles at 0.5 A/g and 5000 cycles at 2 A/g. No noticeable capacity decay was observed as presented in Figure 5d,e, resulting in 100% capacity retention after 150 cycles at 0.5 A/g and 5000 cycles at 2 A/g, indicating that the fabricated porous structure possesses excellent stability. Furthermore, the coulombic efficiency of N-Gr-PE can be maintained at 97% when tested at 0.5 A/g. The higher coulombic efficiency for porous electrodes demonstrates a relatively stable structure for the adsorption/desorption of $AlCl_4^-$ during charge and discharge cycling. Moreover, the SEM image of N-Gr-PE after 100 charge–discharge cycles shows that the porous architecture largely preserved (Figure S13), suggesting good structural stability of the electrode during cycling. To demonstrate the advantage of a porous cathode structure in reducing the resistance in batteries, EIS analysis was performed, and the results are shown in Figure 5f. In the Nyquist plot, the R_{ct} is much lower for the porous N-Gr cathode (397.11 Ω) than N-Gr-DE, consistent with lower interfacial resistance and improved ion accessibility in N-Gr-PE.

To further investigate the energy storage behavior of N-Gr-PE and N-Gr-DE for aluminum battery, CV tests under different scan rates were performed and analyzed. Figure S14 shows the initial five CV curves of N-Gr-PE at a scan rate of 0.1 mV/s. All the curves are well overlapped, demonstrating good reversibility and structural stability. The CV curves of N-Gr-PE and N-Gr-DE show similar shapes with a few weak redox peaks at 2.00, 1.72, and 1.32 V for the cathodic scan and 2.08 V for the anodic scan (Figure 6a). However, the peak positions are different. The large quasi-rectangular shape indicates that the dominant energy storage mechanism in N-Gr-PE and N-Gr-DE is physical adsorption of charge carriers. The cathodic peak positions of N-Gr-PE at 2.00 and 1.32 V are higher than those of the N-Gr-DE (1.90 and 1.30 V); in addition, the potential of the anodic peak of N-Gr-PE at 2.08 V is lower than that of the N-Gr-DE (2.10 V); this

16136829, 0, Downloaded from https://onlinelibrary.wiley.com/doi/10.1002/smll.76627 by Chalmers University Of Technology, Wiley Online Library on [13/11/2026]. See the Terms and Conditions (https://onlinelibrary.wiley.com/terms-and-conditions) on Wiley Online Library for rules of use; OA articles are governed by the applicable Creative Commons License

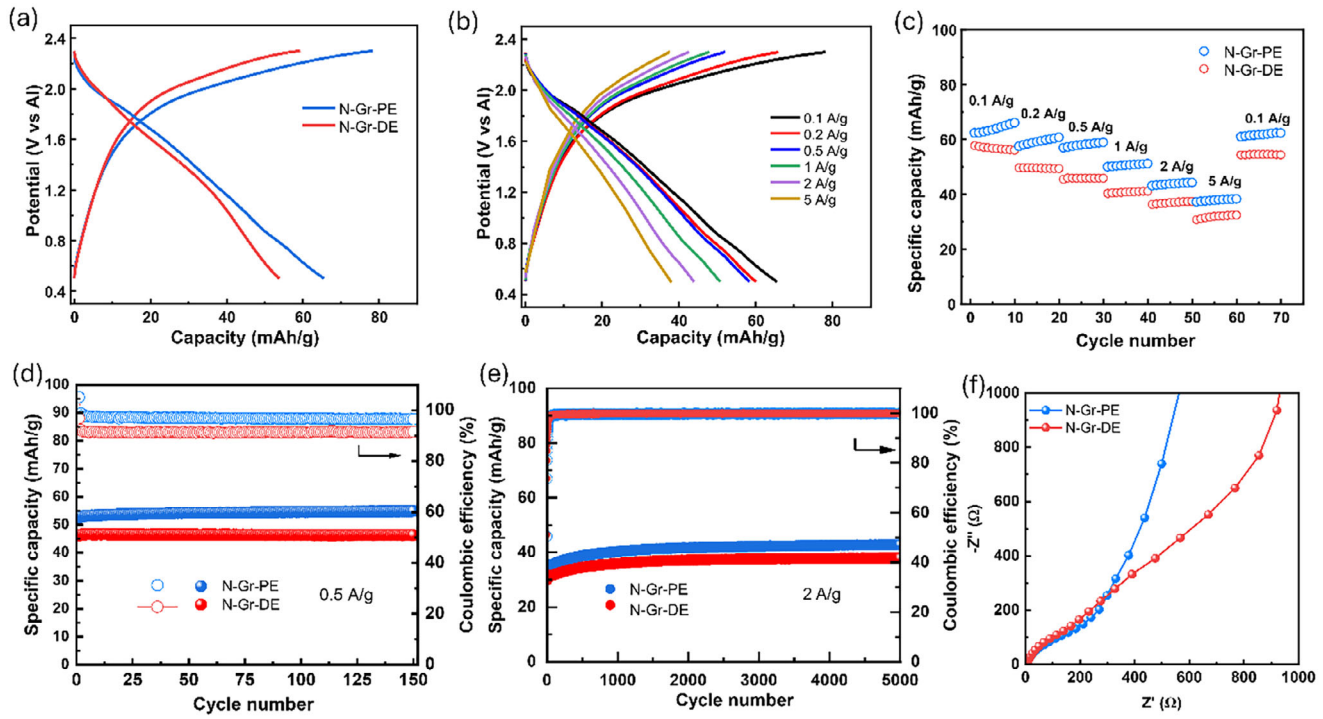


FIGURE 5 | Electrochemical performance of N-Gr porous cathode: (a) The first cycle GCD profiles of N-Gr-PE and N-Gr-DE; (b) GCD profiles of N-Gr-PE for the first cycle at different current densities; (c) Rate capabilities of N-Gr-PE and N-Gr-DE; (d) Cycling performance and Coulombic efficiency of N-Gr-PE and N-Gr-DE at 0.5 A/g for 150 cycles; (e) Cycling performance and Coulombic efficiency of N-Gr-PE and N-Gr-DE at 2 A/g for 5000 cycles; (f) Nyquist plot from EIS measurements for N-Gr-PE and N-Gr-DE.

indicates a fast ion diffusion and more favorable electrode kinetics in the N-Gr-PE, due to the porous structure and ordered N-Gr layers [59, 60].

The mechanism of the electrochemical storage behavior of N-Gr-PE and N-Gr-DE is investigated using CV curves at scan rates of 0.8, 1, 2, 5, and 10 mV/s, as shown in Figure 6b and Figure S15. The electrochemical storage behavior can be explained by two mechanisms: surface-controlled and diffusion dependent current response [61]. To describe the contribution of both mechanisms, Equation (3) is used:

$$i\ (v) = i_{cap} + i_{diff} = k_1\, v + k_2 v^{1/2} \tag{3}$$

where $i(v)$ is the current (mA), v is the different scan rates (mV/s), k_1 and k_2 are the constants [62, 63]. Based on that, the contribution of both mechanisms can be calculated. As an example, in the CV of N-Gr-PE at the scan rate of 2 mV/s (Figure 6c), the blue area corresponds to the surface-controlled capacitance, which is c.a. 81.2% of the total capacity. With the increase of the scan rate from 0.8 to 1, 2, 5, 10 mV/s, the contribution of surface-controlled capacitance also increased from 74.9%, 76.4%, 81.2%, 86.3%, to 91.6% (Figure 6d).

Compared to N-Gr-PE, the surface-controlled contribution in N-Gr-DE is 67.0%, 68.9%, 74.9%, 82.6%, 87.7%, respectively, at the same scan rates (Figures S15 and S16). The higher surface-controlled contribution of N-Gr-PE indicates that a larger fraction of its charge storage is associated with surface-mediated processes. However, this analysis does not, by itself, distinguish among electric double-layer capacitance, pseudocapacitive processes, and specific surface adsorption of $AlCl_4^-$ species. The strategy for creating a porous electrode structure is more important for surface-controlled charge storage because of the enlarged surface area and the electrolyte accommodated within the pores. Consistent with the better rate capability of the porous cathode, the higher surface-controlled contribution of N-Gr-PE suggests that increased accessibility of active sites and improved electrolyte transport enhance $AlCl_4^-$ storage, particularly at high current density. Such plasma-enabled approaches for the heteroatom-doped graphene production with a high number of reactive sites will be beneficial for developing advanced electrode materials for next-generation aluminum batteries.

To further examine the effect of nitrogen incorporation and the porous architectures on the interaction between $AlCl_4^-$ and the graphene framework, *ex situ* Raman measurements were additionally performed for Gr-DE, N-Gr-DE, and N-Gr-PE at selected charge/discharge states (Figure 7a–c and Figure S17). At 2.3 V, Gr-DE exhibits a shoulder in the G-band region, indicating that $AlCl_4^-$ interacts with undoped graphene as well. The corresponding feature becomes more pronounced in N-Gr-DE, suggesting that nitrogen incorporation enhances the interaction of chloroaluminate species with the graphene framework. The porous architecture further increases the accessibility of the associated active sites, as evidenced by a shift in the N-Gr-PE peak, consistent with changes in the graphene electronic/strain state associated with the adsorption of $AlCl_4^-$ on the graphene framework [64]. As the electrode was discharged, the G-band peak shifted back to 1582 cm^{-1} at 1.8 V, and further red shifted to 1573 cm^{-1} at 0.5 V, indicating the reversible removal of the

16136829, 0, Downloaded from https://onlinelibrary.wiley.com/doi/10.1002/smll.76627 by Chalmers University Of Technology, Wiley Online Library on [13/11/2026]. See the Terms and Conditions (https://onlinelibrary.wiley.com/terms-and-conditions) on Wiley Online Library for rules of use; OA articles are governed by the applicable Creative Commons License

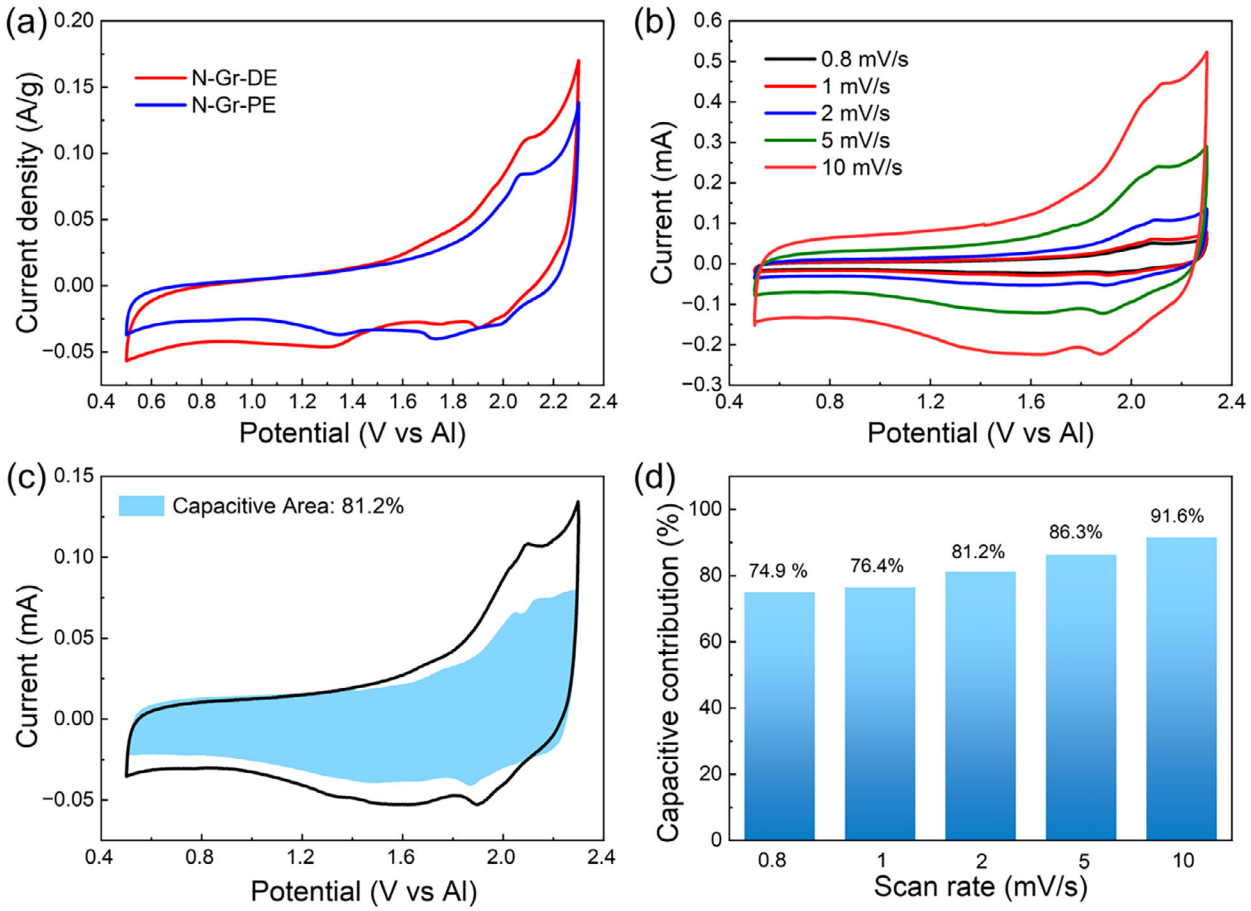


FIGURE 6 | (a) Second cycle CV curves of N-Gr-PE and N-Gr-DE; (b) CV curves at different scan rates for N-Gr-PE; (c) Capacitive-energy-storage contributions of N-Gr-PE at 2 mV/s; (d) Capacitive-energy-storage contributions of N-Gr-PE at different scan rates.

adsorbed $AlCl_4^-$. No significant deviations in the XRD peak positions were observed in the *ex situ* XRD measurements, suggesting that the overall graphene structure is preserved during cycling (Figures S18–S20).

To further investigate the $AlCl_4^-$ storage of N-Gr-PE, *ex situ* XPS was performed to examine the changes of Al, Cl, and C-related peaks in N-Gr-PE during the charging and discharging process. As shown in Figure 7d, the binding energy of the Al 2p peak increased from 74.3 to 74.5 eV when charged from 2.0 to 2.3 V. During the discharge process, the Al 2p peak shifted to a lower binding energy of 74.4 eV at 1.8 V and 74.2 eV at 0.5 V. The peak shift indicates changes in the chemical environment of Al species associated with the adsorption and desorption of $AlCl_4^-$ anions at the N-Gr surface. The Cl 2p spectra (Figure 7e) further support the presence of chloroaluminate species, with the fitted spin-orbit doublets corresponding to different Cl chemical environments. In particular, the additional lower-binding-energy component is consistent with chloroaluminate species interacting strongly with the defect-rich graphene framework [65, 66]. The high-resolution C 1s spectra in Figure 7f provide additional evidence for the reversible interaction between the graphene and chloroaluminate species. The intensity of the fitted component associated with defect-rich carbon at 283.7–284.1 eV increases upon charging to 2.3 V and decreases upon discharge to 0.5 V. Taken together, the *ex situ* Raman and XPS results demonstrate the reversible adsorption and desorption of chloroaluminate species at the N-Gr-PE surface during electrochemical cycling. Combined with the scan-rate-dependent capacitive analysis, these results indicate that the enhanced charge storage of N-Gr-PE is predominantly associated with surface adsorption rather than conventional graphite-like $AlCl_4^-$ intercalation. While the porous architecture improves electrolyte accessibility and ion transport, it can reduce volumetric packing density. Therefore, optimizing pore structure and electrode compaction is important for balancing gravimetric and volumetric performance.

Compared with conventional graphite cathodes, the present N-Gr-PE electrode operates through a different structure–storage mechanism. High-quality graphite can deliver high capacity through highly ordered $AlCl_4^-$ intercalation, whereas the plasma-synthesized N-Gr used here retains a defect-rich graphene framework and exhibits predominantly surface-controlled chloroaluminate storage. The ice-templated porous architecture further increases accessible surface area and electrolyte accessibility, improving the utilization of these surface-active sites. Thus, the present strategy integrates material-level nitrogen doping with electrode-level porous structural engineering to regulate both chloroaluminate interaction and electrolyte accessibility, thereby improving the utilization and rate performance of the graphene cathode. The present approach demonstrates an

16136829, 0, Downloaded from https://onlinelibrary.wiley.com/doi/10.1002/smll.76627 by Chalmers University Of Technology, Wiley Online Library on [13/11/2026]. See the Terms and Conditions (https://onlinelibrary.wiley.com/terms-and-conditions) on Wiley Online Library for rules of use; OA articles are governed by the applicable Creative Commons License

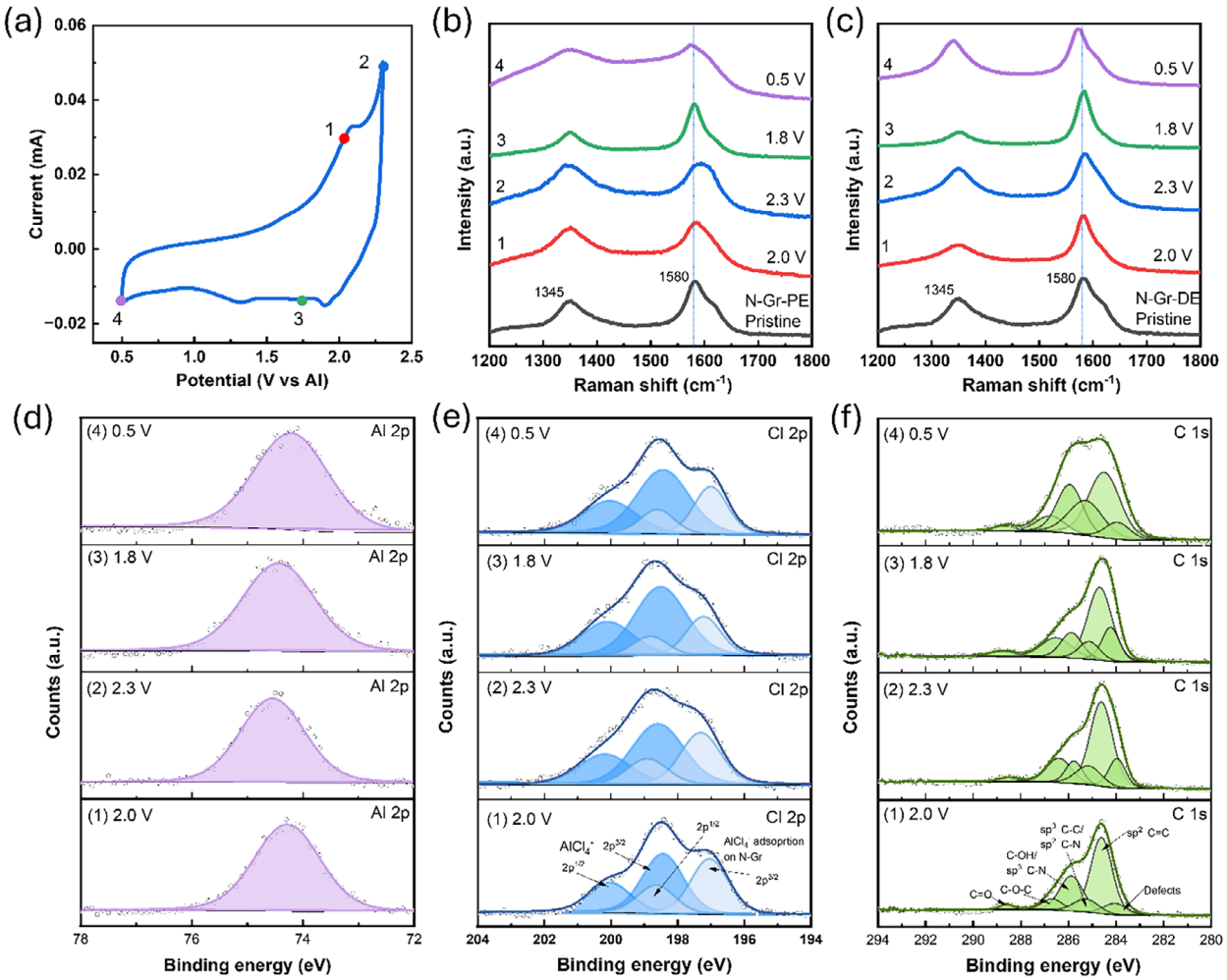


FIGURE 7 | *Ex situ* characterization on N-Gr-PE and N-Gr-DE electrodes: (a) CV curve of N-Gr-DE and N-Gr-PE electrodes for ex situ characterization; *Ex situ* Raman spectra at different voltages during charge-discharge process of (b) N-Gr-PE and (c) N-Gr-DE electrodes; Ex situ XPS spectra of (d) Al 2p, (e) Cl 2p and (f) C 1s of N-Gr-PE at different voltages during charge–discharge process.

effective route to combine heteroatom-modified graphene chemistry with electrode-level structural engineering, particularly for improving the rate performance and utilization of defect-rich graphene electrodes. A comparison with representative carbon cathodes is provided in Table S2.

4 | Conclusions

In summary, we present an effective strategy for the development of high-performance nitrogen-doped porous graphene electrodes for aluminum batteries using an ice-templating approach. Compared with conventional slurry-based electrode fabrication, which typically yields dense structures that hinder ion transport, this method enables the direct formation of three-dimensional porous electrodes. Such architecture significantly enhances ion accessibility, diffusion, and storage kinetics. A low-cost, rapid, and environmentally benign plasma-assisted process was employed to synthesize nitrogen-doped graphene (N-Gr) powder. The ice-templating (freeze-drying) process generates a well-defined porous structure while reducing electrode density, thereby improving electrolyte infiltration and facilitating efficient interaction between the electrolyte and active material. This structural design effectively mitigates the sluggish diffusion of $AlCl_4^-$. Nitrogen doping further enhances performance by increasing the binding affinity of $AlCl_4^-$ and introducing defect sites that act as additional active centers for charge storage. As a result, the synergistic combination of nitrogen doping and porous architecture significantly improves both the physical properties and electrochemical performance of the N-Gr porous electrode. The system demonstrates excellent cycling stability, maintaining 100% capacity retention over 5000 cycles. Quantitatively, nitrogen doping yields a ~50% increase in specific capacity (from 36.24 to 54.4 mAh/g at 0.1 A/g), while the introduction of the porous structure provides an additional ~20% enhancement, achieving 65.5 mAh/g under the same conditions. The engineered porous architecture is particularly critical for graphene-based electrodes, as it enables rapid ion diffusion and increases the availability of active sites for $AlCl_4^-$ storage. The resulting fast electrochemical kinetics are largely governed by adsorption-controlled capacitance, which is confirmed by the *ex situ* Raman and XPS characterization on the electrodes. Overall, this work establishes a robust electrode engineering strategy to overcome diffusion limitations in graphene-based materials, offering a promising pathway for the design of high-performance aluminum batteries.

16136829, 0, Downloaded from https://onlinelibrary.wiley.com/doi/10.1002/smll.76627 by Chalmers University Of Technology, Wiley Online Library on [13/11/2026]. See the Terms and Conditions (https://onlinelibrary.wiley.com/terms-and-conditions) on Wiley Online Library for rules of use; OA articles are governed by the applicable Creative Commons License

Author Contributions

Ruiqi Chen: methodology, investigation, writing – original draft, formal analysis, data curation, validation. **Neelakandan M. Santhosh**: conceptualization, methodology, investigation, validation, formal analysis, data curation, writing – original draft. **Janez Zavašnik**: investigation, formal analysis. **Komal Gola**: methodology, data curation. **Nitish Kumar**: methodology, data curation. **Uta Klement**: validation, writing – original draft. **Eva Kovacevic**: validation, writing – original draft. **Elena Tatarova**: methodology, data curation, validation. **Ana Ferraria**: methodology, validation, data curation. **Vincenzo Palermo**: validation, writing – original draft. **Uroš Cvelbar**: conceptualization, investigation, supervision, resources, writing – original draft, funding acquisition, writing – review and editing, methodology. **Jinhua Sun**: conceptualization, methodology, validation, supervision, resources, project administration, funding acquisition, writing – original draft, writing – review and editing.

Acknowledgements

This work was supported by the EU Graphene Flagship FLAG-ERA III JTC 2021 project "VEGA" (VR-2021-05924, ANR-21-GRF1-0004 or MIZS-PR-11938), Chalmers Area of Advance-Production, 2D TECH VINNOVA competence Center (2019-00068), and GREMI UMR 7344 CNRS& University of Orléans, France. UC, JZ and NMS thank the Slovenian Research Agency (ARIS) for the research program P1-0417 and the project J2-50074. ET acknowledges support by the Portuguese FCT—Fundação para a Ciência e a Tecnologia, through projects UIDB/50010/2020 (https://doi.org/10.54499/UIDB/50010/2020) and UIDP/50010/2020 (https://doi.org/10.54499/UIDP/50010/2020), LA/P/0061/2020 (https://doi.org/10.54499/LA/P/0061/2020); iBB projects UIDB/04565/2020 and UIDP/04565/2020. The work was also supported by the NATO Science for Peace and Security Programme through AEGIS - Advanced Electromagnetic Graphene-based shields via plasma Induced Synthesis, Project (Multi-Year Project G7918). The authors thank Ana Dias for preparing the initial materials.

Conflicts of Interest

The authors declare no conflicts of interest.

Data Availability Statement

The data that support the findings of this study are available on request from the corresponding author. The data are not publicly available due to privacy or ethical restrictions.

References

1. T. Kim, W. Song, D. Y. Son, L. K. Ono, and Y. Qi, "Lithium-ion Batteries: Outlook on Present, Future, and Hybridized Technologies," *Journal of Materials Chemistry A* 7, no. 7 (2019): 2942–2964, https://doi.org/10.1039/C8TA10513H.

2. J. Yan, J. Qian, Y. Li, L. Li, F. Wu, and R. Chen, "Toward Sustainable Lithium Iron Phosphate in Lithium-Ion Batteries: Regeneration Strategies and Their Challenges," *Advanced Functional Materials* 34, no. 44 (2024): 2405055, https://doi.org/10.1002/adfm.202405055.

3. G. Zubi, R. Dufo-López, M. Carvalho, and G. Pasaoglu, "The Lithium-ion Battery: State of the Art and Future Perspectives," *Renewable and Sustainable Energy Reviews* 89 (2018): 292–308, https://doi.org/10.1016/j.rser.2018.03.002.

4. X. Xu, X. Han, L. Lu, et al., "Challenges and Opportunities Toward Long-life Lithium-ion Batteries," *Journal of Power Sources* 603 (2024): 234445, https://doi.org/10.1016/j.jpowsour.2024.234445.

5. N. Nasajpour-Esfahani, H. Garmestani, M. Bagheritabar, et al., "Comprehensive Review of Lithium-ion Battery Materials and Development Challenges," *Renewable and Sustainable Energy Reviews* 203 (2024): 114783, https://doi.org/10.1016/j.rser.2024.114783.

6. B. Johansson, M. Despeisse, J. Bokrantz, et al., "Challenges and Opportunities to Advance Manufacturing Research for Sustainable Battery Life Cycles," *Frontiers in Manufacturing Technology* 4 (2024): 2024.

7. Y. Sun, J. Sun, J. S. Sanchez, et al., "Surface Chemistry and Structure Manipulation of Graphene-related Materials to Address the Challenges of Electrochemical Energy Storage," *Chemical Communications* 59, no. 18 (2023): 2571–2583, https://doi.org/10.1039/D2CC06772B.

8. J. Sun, M. Sadd, P. Edenborg, et al., "Real-time imaging of Na + reversible intercalation in "Janus" graphene stacks for battery applications," *Science Advances* 7, no. 22 (2021): abf0812, https://doi.org/10.1126/sciadv.abf0812.

9. J. Sun, J. Y. Hwang, P. Jankowski, et al., "Critical Role of Functional Groups Containing N, S, and O on Graphene Surface for Stable and Fast Charging Li-S Batteries," *Small* 17, no. 17 (2021): 2007242.

10. W. Pan, Y. Wang, Y. Zhang, et al., "A Low-cost and Dendrite-free Rechargeable Aluminium-ion Battery With Superior Performance," *Journal of Materials Chemistry A* 7, no. 29 (2019): 17420–17425, https://doi.org/10.1039/C9TA05207K.

11. D. Y. Wang, C. Y. Wei, M. C. Lin, et al., "Advanced Rechargeable Aluminium Ion Battery With a High-quality Natural Graphite Cathode," *Nature Communications* 8, no. 1 (2017): 14283, https://doi.org/10.1038/ncomms14283.

12. E. Hu, B. E. Jia, W. Nong, et al., "Boosting Aluminum Adsorption and Deposition on Single-Atom Catalysts in Aqueous Aluminum-Ion Battery," *Advanced Energy Materials* 14, no. 34 (2024): 2401598, https://doi.org/10.1002/aenm.202401598.

13. P. Thanwisai, N. Chaiyapo, P. Phuenhinlad, et al., "Mesoporous and Defective Activated Carbon Cathode for AlCl4− Anion Storage in Non-aqueous Aluminium-ion Batteries," *Carbon* 191 (2022): 195–204, https://doi.org/10.1016/j.carbon.2022.01.063.

14. B. E. Jia, A. Q. Thang, C. Yan, et al., "Rechargeable Aqueous Aluminum-Ion Battery: Progress and Outlook," *Small* 18, no. 43 (2022): 2107773.

15. M. C. Lin, M. Gong, B. Lu, et al., "An Ultrafast Rechargeable Aluminium-ion Battery," *Nature* 520, no. 7547 (2015): 324–328, https://doi.org/10.1038/nature14340.

16. A. K. Geim, "Graphene: Status and Prospects," *Science* 324, no. 5934 (2009): 1530–1534, https://doi.org/10.1126/science.1158877.

17. S. K. Das, "Graphene: A Cathode Material of Choice for Aluminum-Ion Batteries," *Angewandte Chemie International Edition* 57, no. 51 (2018): 16606–16617, https://doi.org/10.1002/anie.201802595.

18. H. Chen, F. Guo, Y. Liu, et al., "A Defect-Free Principle for Advanced Graphene Cathode of Aluminum-Ion Battery," *Advanced Materials* 29, no. 12 (2017): 1605958, https://doi.org/10.1002/adma.201605958.

19. H. Chen, H. Xu, S. Wang, et al., "Ultrafast all-climate Aluminum-graphene Battery With Quarter-million Cycle Life," *Science Advances* 3, no. 12 (2017): aao7233, https://doi.org/10.1126/sciadv.aao7233.

20. R. Munoz and C. Gómez-Aleixandre, "Review of CVD Synthesis of Graphene," *Chemical Vapor Deposition* 19, no. 10-11-12 (2013): 297–322, https://doi.org/10.1002/cvde.201300051.

21. B. Deng, Z. Liu, and H. Peng, "Toward Mass Production of CVD Graphene Films," *Advanced Materials* 31, no. 9 (2019): 1800996, https://doi.org/10.1002/adma.201800996.

22. N. M. Santhosh, G. Filipič, E. Tatarova, et al., "Oriented Carbon Nanostructures by Plasma Processing: Recent Advances and Future Challenges," *Micromachines* 9, no. 11 (2018): 565.

23. N. M. Santhosh, G. Filipic, E. Kovacevic, et al., "N-Graphene Nanowalls via Plasma Nitrogen Incorporation and Substitution: The Experimental Evidence," *Nano-Micro Letters* 12, no. 1 (2020): 53, https://doi.org/10.1007/s40820-020-0395-5.

16136829, 0, Downloaded from https://onlinelibrary.wiley.com/doi/10.1002/smll.76627 by Chalmers University Of Technology, Wiley Online Library on [13/11/2026]. See the Terms and Conditions (https://onlinelibrary.wiley.com/terms-and-conditions) on Wiley Online Library for rules of use; OA articles are governed by the applicable Creative Commons License

24. N. M. Santhosh, K. K. Upadhyay, P. Stražar, et al., "Advanced Carbon–Nickel Sulfide Hybrid Nanostructures: Extending the Limits of Battery-Type Electrodes for Redox-Based Supercapacitor Applications," *ACS Applied Materials & Interfaces* 13, no. 17 (2021): 20559–20572, https://doi.org/10.1021/acsami.1c03053.

25. J. Sun, F. Morales-Lara, A. Klechikov, et al., "Porous Graphite Oxide Pillared With Tetrapod-shaped Molecules," *Carbon* 120 (2017): 145–156, https://doi.org/10.1016/j.carbon.2017.05.007.

26. Y. Xie, Z. Meng, T. Cai, and W. Q. Han, "Effect of Boron-Doping on the Graphene Aerogel Used as Cathode for the Lithium–Sulfur Battery," *ACS Applied Materials & Interfaces* 7, no. 45 (2015): 25202–25210, https://doi.org/10.1021/acsami.5b08129.

27. Z. S. Wu, A. Winter, L. Chen, et al., "Three-Dimensional Nitrogen and Boron Co-doped Graphene for High-Performance All-Solid-State Supercapacitors," *Advanced Materials* 24, no. 37 (2012): 5130–5135, https://doi.org/10.1002/adma.201201948.

28. Y. Du, B. Zhang, R. Kang, et al., "Boron-doping-induced Defect Engineering Enables High Performance of a Graphene Cathode for Aluminum Batteries," *Inorganic Chemistry Frontiers* 2, no. 5 (2022): 925–934, https://doi.org/10.1039/D1QI01474A.

29. A. Childress, P. Parajuli, S. Eyley, W. Thielemans, R. Podila, and A. M. Rao, "Effect of Nitrogen Doping in the Few Layer Graphene Cathode of an Aluminum Ion Battery," *Chemical Physics Letters* 733 (2019): 136669, https://doi.org/10.1016/j.cplett.2019.136669.

30. S. Sakulsermsuk, P. Singjai, and C. Chaiwong, "Influence of Plasma Process on the Nitrogen Configuration in Graphene," *Diamond and Related Materials* 70 (2016): 211–218, https://doi.org/10.1016/j.diamond.2016.11.001.

31. A. S. Childress, P. Parajuli, J. Zhu, R. Podila, and A. M. Rao, "A Raman Spectroscopic Study of Graphene Cathodes in High-performance Aluminum Ion Batteries," *Nano Energy* 39 (2017): 69–76, https://doi.org/10.1016/j.nanoen.2017.06.038.

32. M. Rybin, A. Pereyaslavtsev, T. Vasilieva, et al., "Efficient Nitrogen Doping of Graphene by Plasma Treatment," *Carbon* 96 (2016): 196–202, https://doi.org/10.1016/j.carbon.2015.09.056.

33. N. Bundaleska, A. Dias, N. Bundaleski, et al., "Prospects for Microwave Plasma Synthesized N-graphene in Secondary Electron Emission Mitigation Applications," *Scientific Reports* 10, no. 1 (2020): 13013, https://doi.org/10.1038/s41598-020-69844-9.

34. Z. Wang, D. Zhang, X. Bao, et al., "Space-confined Intercalation Expansion Strategy for Simple and Rapid Synthesis of kish-based Expanded Graphite for Aluminum Ion Batteries," *Carbon* 223 (2024): 119016, https://doi.org/10.1016/j.carbon.2024.119016.

35. Y. Kong, C. Tang, X. Huang, et al., "Thermal Reductive Perforation of Graphene Cathode for High-Performance Aluminum-Ion Batteries," *Advanced Functional Materials* 31, no. 17 (2021): 2010569, https://doi.org/10.1002/adfm.202010569.

36. Y. Zhao, B. Liu, Y. Yi, et al., "An Anode-Free Potassium-Metal Battery Enabled by a Directly Grown Graphene-Modulated Aluminum Current Collector," *Advanced Materials* 34, no. 29 (2022): 2202902, https://doi.org/10.1002/adma.202202902.

37. Y. Yi, J. Li, Z. Gao, et al., "Highly Potassiophilic Graphdiyne Skeletons Decorated With Cu Quantum Dots Enable Dendrite-Free Potassium-Metal Anodes," *Advanced Materials* 34, no. 29 (2022): 2202685, https://doi.org/10.1002/adma.202202685.

38. Z. Meng, Y. Zou, J. Chen, et al., "Overcoming Passivation–Corrosion Dilemma of Al Current Collector for Aqueous Zn Battery," *ACS nano* 20, no. 13 (2026): 10745–10754, https://doi.org/10.1021/acsnano.6c02382.

39. H. Ci, C. Hao, J. Yang, et al., "High Capacity Output via all-carbon Host in Current Collector-free Li-S Batteries," *Journal of Energy Chemistry* 116 (2026): 736–743, https://doi.org/10.1016/j.jechem.2026.01.028.

40. X. Lian, Y. Wu, J. Li, et al., "Grain-Boundary-Enriched SEI via Field Regulation Enables Anode-Less Potassium Metal Batteries," *Advanced Functional Materials* 36, no. 35 (2026): 28259, https://doi.org/10.1002/adfm.202528259.

41. L. Wang, G. Zhu, Y. Lin, Y. Wang, Q. Zhu, and Z. Dai, "MOF-derived Hierarchical Porous Carbon Octahedrons for Aluminum-ion Batteries," *Carbon* 202 (2023): 305–313, https://doi.org/10.1016/j.carbon.2022.10.069.

42. J. Sun, M. A. Memon, W. Bai, et al., "Controllable Fabrication of Transparent Macroporous Graphene Thin Films and Versatile Applications as a Conducting Platform," *Advanced Functional Materials* 25, no. 27 (2015): 4334–4343, https://doi.org/10.1002/adfm.201501733.

43. J. Sun, L. Xiao, S. Jiang, G. Li, Y. Huang, and J. Geng, "Fluorine-Doped SnO_2@Graphene Porous Composite for High Capacity Lithium-Ion Batteries," *Chemistry of Materials* 27, no. 13 (2015): 4594–4603, https://doi.org/10.1021/acs.chemmater.5b00885.

44. H. Huang, F. Zhou, X. Shi, et al., "Graphene Aerogel Derived Compact Films for Ultrafast and High-capacity Aluminum Ion Batteries," *Energy Storage Materials* 23 (2019): 664–669, https://doi.org/10.1016/j.ensm.2019.03.001.

45. E. Tatarova, A. Dias, J. Henriques, et al., "Towards Large-scale in Free-standing Graphene and N-graphene Sheets," *Scientific Reports* 7, no. 1 (2017): 10175, https://doi.org/10.1038/s41598-017-10810-3.

46. N. Bundaleska, J. Henriques, M. Abrashev, et al., "Large-scale Synthesis of Free-standing N-doped Graphene Using Microwave Plasma," *Scientific Reports* 8, no. 1 (2018): 12595, https://doi.org/10.1038/s41598-018-30870-3.

47. A. C. Ferrari and D. M. Basko, "Raman Spectroscopy as a Versatile Tool for Studying the Properties of Graphene," *Nature Nanotechnology* 8, no. 4 (2013): 235–246, https://doi.org/10.1038/nnano.2013.46.

48. R. Bigras, X. Glad, P. Vinchon, R. Martel, and L. Stafford, "Selective nitrogen doping of graphene due to preferential healing of plasma-generated defects near grain boundaries," *npj 2D Materials and Applications* 4, no. 1 (2020): 42.

49. B. J. Matsoso, K. Ranganathan, B. K. Mutuma, T. Lerotholi, G. Jones, and N. J. Coville, "Time-Dependent Evolution Of The Nitrogen Configurations in N-doped Graphene Films," *RSC Advances* 6, no. 108 (2016): 106914–106920.

50. M. Santhosh, K. K. Upadhyay, G. Filipič, J. Zavašnik, M. de Fátima Montemor, and U. Cvelbar, "Widening the Limit of Capacitance at High Frequency for AC Line-filtering Applications Using Aqueous Carbon-based Supercapacitors," *Carbon* 203 (2023): 686–694, https://doi.org/10.1016/j.carbon.2022.12.026.

51. A. S. Dobrota, J. Vlahović, N. V. Skorodumova, and I. A. Pašti, "First-Principles Analysis Of Aluminium Interaction With nitrogen-Doped Graphene Nanoribbons—From Adatom Bonding To Various Potential Applications," *Materials Today Communications* 31 (2022): 103388, https://doi.org/10.1016/j.mtcomm.2022.103388.

52. S. Wang, S. Jiao, W. L. Song, et al., "A Novel Dual-graphite Aluminum-ion Battery," *Energy Storage Materials* 12 (2018): 119–127, https://doi.org/10.1016/j.ensm.2017.12.010.

53. Y. Chen, H. Suzuki, S. Fukumoto, et al., "Enhanced Capacity of Aluminum-ion Batteries by Adjusting the Average Pore Size of the Porous Carbon Cathode," *Journal of Materials Chemistry A* 13 (2025): 8052–8058.

54. I. Yang, S. G. Kim, S. H. Kwon, M. S. Kim, and J. C. Jung, "Relationships Between Pore Size and Charge Transfer Resistance of Carbon Aerogels for Organic Electric Double-layer Capacitor Electrodes," *Electrochimica Acta* 223 (2017): 21–30, https://doi.org/10.1016/j.electacta.2016.11.177.

55. S. Phulpoto, J. Sun, S. Qi, L. Xiao, S. Yan, and J. Geng, "Tuning the Morphologies of Fluorine-doped Tin Oxides in the Three-dimensional Architecture of Graphene for High-performance Lithium-ion Batteries," *Nanotechnology* 28, no. 39 (2017): 395404, https://doi.org/10.1088/1361-6528/aa8106.

56. J. Sun, A. Klechikov, C. Moise, M. Prodana, M. Enachescu, and A. V. Talyzin, "A Molecular Pillar Approach To Grow Vertical Covalent

16136829, 0, Downloaded from https://onlinelibrary.wiley.com/doi/10.1002/smll.76627 by Chalmers University Of Technology, Wiley Online Library on [13/11/2026]. See the Terms and Conditions (https://onlinelibrary.wiley.com/terms-and-conditions) on Wiley Online Library for rules of use; OA articles are governed by the applicable Creative Commons License

Organic Framework Nanosheets on Graphene: Hybrid Materials for Energy Storage," *Angewandte Chemie International Edition* 57, no. 4 (2018): 1034–1038, https://doi.org/10.1002/anie.201710502.

57. Y. Wu, M. Gong, M. C. Lin, et al., "3D Graphitic Foams Derived From Chloroaluminate Anion Intercalation for Ultrafast Aluminum-Ion Battery," *Advanced Materials* 28, no. 41 (2016): 9218–9222, https://doi.org/10.1002/adma.201602958.

58. J. Zhong, W. Sun, Q. Wei, X. Qian, H. M. Cheng, and W. Ren, "Efficient and Scalable Synthesis of Highly Aligned and Compact Two-dimensional Nanosheet Films With Record Performances," *Nature Communications* 9, no. 1 (2018): 3484, https://doi.org/10.1038/s41467-018-05723-2.

59. C. Li, X. Zhang, K. Wang, et al., "Nitrogen-enriched Graphene Framework From a Large-scale Magnesiothermic Conversion of CO_2 With Synergistic Kinetics for High-power Lithium-ion Capacitors," *NPG Asia Materials* 13, no. 1 (2021): 59, https://doi.org/10.1038/s41427-021-00327-7.

60. F. Han, W. Jing, Q. Wu, et al., "Nitrogen-doped Graphene fiber Electrodes With Optimal Micro-/Meso-/Macro-porosity Ratios for High-performance Flexible Supercapacitors," *Journal of Power Sources* 520 (2022): 230866, https://doi.org/10.1016/j.jpowsour.2021.230866.

61. D. Chao, C. Zhu, P. Yang, et al., "Array of Nanosheets Render Ultrafast and High-capacity Na-ion Storage by Tunable Pseudocapacitance," *Nature Communications* 7, no. 1 (2016): 12122, https://doi.org/10.1038/ncomms12122.

62. P. Simon, Y. Gogotsi, and B. Dunn, "Where Do Batteries End and Supercapacitors Begin?," *Science* 343, no. 6176 (2014): 1210–1211, https://doi.org/10.1126/science.1249625.

63. T. C. Liu, W. Pell, B. Conway, and S. Roberson, "Behavior of Molybdenum Nitrides as Materials for Electrochemical Capacitors: Comparison With Ruthenium Oxide," *Journal of the Electrochemical Society* 145, no. 6 (1998): 1882–1888, https://doi.org/10.1149/1.1838571.

64. Z. H. Ni, T. Yu, Y. H. Lu, Y. Y. Wang, Y. P. Feng, and Z. X. Shen, "Uniaxial Strain on Graphene: Raman Spectroscopy Study and Band-gap Opening," *ACS nano* 2, no. 11 (2008): 2301–2305, https://doi.org/10.1021/nn800459e.

65. D. J. Yoo, M. Heeney, F. Glöcklhofer, and J. Choi, "Tetradiketone Macrocycle for Divalent Aluminium Ion Batteries," *Nature Communications* 12 (2021): 23386.

66. R. Garcia-Mendez, J. Zheng, D. Bock, et al., "Understanding The Reversible Electrodeposition of Al in Low-Cost Room Temperature Molten Salts," *Cell Reports Physical Science* 4 (2023): 101452.

Supporting Information

Additional supporting information can be found online in the Supporting Information section.

Supporting File: smll76627-sup-0001-SuppMat.docx.

16136829, 0, Downloaded from https://onlinelibrary.wiley.com/doi/10.1002/smll.76627 by Chalmers University Of Technology, Wiley Online Library on [13/11/2026]. See the Terms and Conditions (https://onlinelibrary.wiley.com/terms-and-conditions) on Wiley Online Library for rules of use; OA articles are governed by the applicable Creative Commons License